Molecular Imaging and Biology (2023) 25:391–400
https://doi.org/10.1007/s11307-022-01769-3

RESEARCH ARTICLE

Diagnostic and Dosimetry Features of [^{64}Cu]$CuCl_2$ in High-Grade Paediatric Infiltrative Gliomas

Francesco Fiz[1] · Gianluca Bottoni[1] · Martina Ugolini[1] · Sergio Righi[2] · Alessio Cirone[2] · Maria Carmen Garganese[3] · Antonio Verrico[4] · Andrea Rossi[5,6] · Claudia Milanaccio[4] · Antonia Ramaglia[5] · Angela Mastronuzzi[7] · Massimo Eraldo Abate[8] · Antonella Cacchione[7] · Carlo Gandolfo[9] · Giovanna Stefania Colafati[9] · Maria Luisa Garrè[4] · Giovanni Morana[10] · Arnoldo Piccardo[1]

Received: 18 May 2022 / Revised: 10 August 2022 / Accepted: 18 August 2022 / Published online: 30 August 2022

Abstract

Purpose of the Report Paediatric diffuse high-grade gliomas (PDHGG) are rare central nervous system neoplasms lacking effective therapeutic options. Molecular imaging of tumour metabolism might identify novel diagnostic/therapeutic targets. In this study, we evaluated the distribution and the dosimetry aspects of [^{64}Cu]$CuCl_2$ in PDHGG subjects, as copper is a key element in cellular metabolism whose turnover may be increased in tumour cells.

Material and Methods Paediatric patients with PDHGG were prospectively recruited. [^{64}Cu]$CuCl_2$ PET/CT was performed 1 h after tracer injection; if the scan was positive, it was repeated 24 and 72 h later. Lesion standardised uptake value (SUV) and target-to-background ratio (TBR) were calculated. Tumour and organ dosimetry were computed using the MIRD algorithm. Each patient underwent an MRI scan, including FLAIR, T2-weighted and post-contrast T1-weighted imaging.

Results Ten patients were enrolled (median age 9, range 6–16 years, 6 females). Diagnoses were diffuse midline gliomas ($n=8$, 5 of which with H3K27 alterations) and diffuse hemispheric gliomas ($n=2$). Six patients had visible tracer uptake (SUV: 1.0 ± 0.6 TBR: 5 ± 3.1). [^{64}Cu]$CuCl_2$ accumulation was always concordant with MRI contrast enhancement and was higher in the presence of radiological signs of necrosis. SUV and TBR progressively increased on the 24- and 72-h acquisitions ($p<0.05$ and $p<0.01$, respectively). The liver and the abdominal organs received the highest non-target dose.

Conclusions [^{64}Cu]$CuCl_2$ is a well-tolerated radiotracer with reasonably favourable dosimetric properties, showing selective uptake in tumour areas with visible contrast enhancement and necrosis, thus suggesting that blood–brain barrier damage is a pre-requisite for its distribution to the intracranial structures. Moreover, tracer uptake showed an accumulating trend over time. These characteristics could deserve further analysis, to determine whether this radiopharmaceutical might have a possible therapeutic role as well.

Key words Copper · [^{64}Cu]$CuCl^2$ · PET/CT · Gliomas · Paediatrics

Introduction

Paediatric gliomas are the most common central nervous system neoplasms in children [1]. Unlike their adult counterparts, paediatric-type diffuse high-grade gliomas (PDHGG) are rare, accounting for only 5–20% of all gliomas [2–4]. The prognosis of these forms is dismal, with median overall survival ranging between 9 and 16 months for PDHGG and less than 1 year for diffuse intrinsic pontine glioma (DIPG) [3, 5–9].

Complete surgical resection of these infiltrative tumours is virtually impossible, and surgery is typically not attempted in patients with DIPG, owing to the location of the tumour [10–12]. Concurrent adjuvant radiotherapy, in combination with chemotherapy, is the standard of care for newly diagnosed PDHGG, but still less than 5% of patients survive longer than 5 years post-diagnosis [13, 14]. Since no chemotherapeutic drugs have proven effective in the treatment of DIPG, radiation therapy is the current standard regimen [15–18].

Giovanni Morana and Arnoldo Piccardo share senior co-authorship.

✉ Francesco Fiz
francesco.fiz.nm@gmail.com

Extended author information available on the last page of the article

Despite dramatic improvements in the genetic and epigenetic analyses of PDHGG [4], we are still in the early stages of developing gene-targeted therapies. An alternative approach is to focus on the tumour cell metabolism; in this context, molecular imaging could provide additional information on the biological behaviour of the tumour and possibly identify new targets for a tailored approach [19, 20]. Copper is a key element in cellular turnover, being a vital co-enzyme in a number of cell functions, including mitochondrial respiration [21, 22]. Unsurprisingly, this element plays a major role in tumorigenesis and in cancer metabolism; more specifically, it has been found that copper is linked with mitogen-activated kinase stimulation and, in particular, with BRAF and K-RAS [23–25]. Moreover, copper is involved in cancer mitochondria-dependent energy production [26], tumour invasiveness, and even chemotherapy resistance [27]. By contrast, the normal brain parenchyma has little need for this element. Imaging aggressive brain neoplasms with a copper radioisotope might provide a favourable target-to-background ratio.

In particular, ^{64}Cu could play both diagnostic and therapeutic roles, as its decay scheme entails the production of positrons, high-energy beta particles and Auger electrons with high linear energy transfer (LET) [28–30]. Indeed, this high-LET radiation could play the most important role in the theranostic effect of [^{64}Cu]$CuCl_2$ [31]. This tracer [^{64}Cu]$CuCl_2$ PET/CT has been proposed as a promising procedure for identifying adult high-grade gliomas, which often display intense tracer uptake [32].

This pilot trial aimed to evaluate the potential diagnostic role of [^{64}Cu]$CuCl_2$ PET/CT in patients with PDHGG by comparing PET images with MRI. We aimed to estimate kinetics, tumour/background ratio (TBR) over time, the absorbed dose of [^{64}Cu]$CuCl_2$ in gliomas and in organs, as well as the effective dose.

Material and Methods

Radiopharmaceutical

Copper-64 dichloride ([^{64}Cu]$CuCl_2$, average specific activity, 3700 MBq/µg, radiochemical purity > 99%, radionuclide purity > 99%) was produced according to a procedure previously reported [32, 33]. Briefly, ^{64}Cu was produced by bombarding an electroplated ^{64}Ni target using a proton current of 18 µA and energy of 14.6 MeV. Following bombardment, ^{64}Cu was purified from other contaminants by means of chromatography and an ion-exchange column (Biorad Laboratories). The radioisotope was eluted with concentrated HCl and sieved through a 0.2-µm filter (Merck Millipore). Radionuclide purity and ^{64}Cu half-life were measured by means of an HPGe detector (Ortec), by identifying the characteristic 511, 1022, and 1345.8 keV photopeaks. A radionuclide purity ≥ 99.5% was considered acceptable. Radiochemical purity (RCP) was assessed by having [^{64}Cu]$CuCl_2$ react with the tetraazacyclotetradecane-N, N′, N″, N‴-tetraacetic acid ligand; a purity ≥ 99% was deemed acceptable.

Patient Population and Diagnostic Protocol

The local ethics committee (Comitato Etico Regionale Liguria Registration Number: 076/2019) and the "Agenzia Italiana del Farmaco" (Italian Drug Agency) approved this study. All children's legal guardians signed a written informed consent form. The trial was registered in the European Clinical Trial Database (EudraCT number 2018–004,667-30). The neuro-oncological departments of three Italian children's hospitals (Istituto G. Gaslini in Genoa, Bambino Gesù Children's Hospital in Rome and AORN Santobono-Pausilipon Hospital in Naples) prospectively enrolled patients with recurrent/progressive PDHGG according to the inclusion/exclusion criteria (Table 1).

[^{64}Cu]$CuCl_2$ was injected into a cubital vein (median activity: 179 MBq, range 113–280 MBq, corresponding to a median of 3.9 MBq/kg, range 2.4–9.4 MBq/kg). Brain PET/CT acquisition was started 60 min thereafter and lasted 30 min. Subsequently, whole-body PET acquisition was started. Further acquisitions (i.e., brain and whole-body) were performed 24 and 72 h after the injection. In all patients, an MRI examination, including fluid attenuation inversion recovery (FLAIR), T2-weighted and pre- and post-contrast (0.1 mmol/kg, macrocyclic ionic agent) T1-weighted images, was performed. All patients were acquired on a Discovery ST PET/CT device (General Electric Healthcare Technologies, Milwaukee, WI, USA) and on a 1.5 Tesla MRI scanner (Intera Achieva, Philips, Best, the Netherlands).

Image Analysis: Registration and Voi Segmentation

PET/CT images were evaluated visually and semi-quantitatively in a patient-by-patient and lesion-by-lesion analysis after fusion of the images with MRI images (T1, T2 and FLAIR). Fusion was obtained automatically by means of a commercially available image-registration software tool (AW Server, General Electric Medical Systems). As previously described [31], volumes of interest (VOIs) were constructed on the L4-L5 vertebral bodies to assess the biokinetics and dosimetry of the active bone marrow. Subsequently, the active bone marrow in the whole body was calculated as a function of body weight [34]. VOIs were also delineated at the venous access site, to estimate the net activity administered.

In our analysis, the [^{64}Cu]$CuCl_2$ PET detection rate (DR) was defined as the ability to detect at least one

Table 1 Inclusion and exclusion criteria of the population

Inclusion criteria
Pathologically confirmed PDHGG. DIPG according to clinical and MRI criteria (T1 hypointense and T2 hyperintense diffusely infiltrating lesion arising in and involving ≥ 50% of the pons)
At least one morphologically measurable lesion (1-cm main axis)
Karnofsky performance status ≥ 60
Expected survival ≥ 3 months
Age between 5 and 18 years
Normal bone marrow function (absolute neutrophil count ≥ 1.5 × 109/L; platelets ≥ 150/nl; haemoglobin ≥ 9 g/L)
Adequate hepatic function, i.e.: (a) liver enzymes ≤ 2.5 times the upper normal limit, direct bilirubin ≤ 1.5 times the upper normal limit; (b) normal ALP values; (c) normal coagulation parameters
Normal renal function (creatinine ≤ 1.5 mg/dl or creatinine clearance ≥ 60 ml/min)
Undetectable hCG in fertile female subject or proven inability to conceive
Written informed consent (must be signed before any study-related procedure)
Full capacity to understand the study procedures
Exclusion criteria
Findings not compatible with PDHGG on pathology or with DIPG on imaging
Contraindications for MRI contrast medium
Copper metabolism disorders (e.g., Wilson's or Menkes' disease)
Uncontrolled concomitant systemic condition (e.g., active infection, congestive heart failure, unstable angina pectoris, cardiac arrythmias, psychic conditions affecting patients' compliance, uncontrolled diabetes)
Pregnancy or breastfeeding
Sexually active subjects not using birth control
HIV-positive subjects; patients with acquired immunodeficiency syndrome or HBV/HCV-positivity

pathological finding in each individual subject. The characteristics and extent of the tumour on conventional MRI were also correlated with [^{64}Cu]$CuCl_2$ PET uptake. Given the diffuse nature of the disease, tumour extent was delineated on the basis of T2/FLAIR MRI signal abnormalities. Any area of contrast enhancement within each lesion was also reviewed and correlated with [^{64}Cu]$CuCl_2$ PET uptake.

PET/CT was rated as positive if tumours identified on MRI exhibited tracer uptake above the level of the corresponding contralateral or remote normal brain tissue.

Kinetics of Tumours and Organs

The activity concentration of [^{64}Cu]$CuCl_2$ (as a percentage of injected activity/ml) in VOIs of tumours and organs for all PET datasets was recorded and fitted to a mono-exponential function or with the trapezoidal methods [35]. Hence, the time-integrated activity and its coefficient were determined. The mean activity concentration inside the tumour was corrected for the partial volume effect (PVE), as previously described [31]. The protocol is based on numerical recovery coefficients that are experimentally derived by using radioactive phantoms. Finally, the average standardised uptake values (SUV) in tumours over time was calculated and expressed as mean ± standard deviation.

Tumour/Background Ratio (TBR)

The tumour-to-background ratio (TBR) of all lesions was defined as the relation between the mean activity concentration of the lesion and the one of the background tissue; it was expressed as mean ± standard deviation. The background radioactivity concentration was obtained by calculating the mean value of VOIs drawn at 1-cm distance from each detectable lesion, at the four cardinal points.

Dosimetry of Tumours and Organs

Tumour and organ dosimetry was carried out by calculating the absorbed dose coefficient (absorbed dose per administered activity) according to the Medical Internal Radiation Dose (MIRD) system [36, 37]. The OLINDA/EXM dosimetry software was used to calculate mean organ absorbed doses based on reference anatomic models, including the reference newborn, 1-year-old, 5-year-old, 10-year-old, 15-year-old, and adult female and adult male [38]. Tumour dosimetry was calculated with the dose factors of sphere-shaped phantoms. Finally, the absorbed dose coefficients were obtained by multiplying the dose factors by the time-integrated activity coefficients. The effective dose was calculated on the basis of the tissue weighting factors of the organs (ICRP protocols 60 and 103) [39, 40].

Results

Patient Population

We prospectively enrolled ten patients (median age 9, range 6–16 years, 6 females), according to the inclusion criteria (Table 1). All patients had a Karnofsky performance status above 80%. Injection of the radiopharmaceutical was well tolerated, and no immediate or late side DIPG was established on the basis of clinical and MRI criteria, in accordance with RAPNO guidelines [41]. In two subjects with diffuse high-grade hemispheric gliomas, the WHO grade was determined according to histological features, owing to the lack of molecular information. Most patients ($n = 8$) were affected by diffuse midline gliomas (five H3K27-altered). Six of the ten patients had a positive [^{64}Cu]$CuCl_2$ PET/CT scan (all patients' characteristics are reported in Table 2). In all patients, no uptake was detected in the normal parenchyma, while intense uptake was observed in the structures located outside the blood–brain barrier (e.g., choroid plexus and hypophysis) (Fig. 1).

Diagnostic Evaluation and Lesion Analysis

On MR imaging, all gliomas showed increased T2/FLAIR signal intensity and variable (iso- to hypointense) appearance on T1-weighted imaging. After administration of contrast material, six tumours displayed contrast enhancement [eight contrast-enhancing areas, five of which exhibited signs of necrosis (ring-shaped enhancement)].

Table 2 General characteristics of the patient population

Subject no	Sex	Age (y)	Weight (kg)	Adm. activity (MBq)	Diagnosis	Location	MRI contrast enhancement	MRI necrotic areas	$^{64}CuCl_2$ uptake
1	F	6	21	180	DPHGG, H3-wildtype, and IDH-wildtype	Pons	Y	N	Y
2	F	6	22	206	DMG, H3 K27-altered	Pons	N	N	N
3	F	15	56	231	DPHGG, H3-wildtype, and IDH-wildtype	Th	N	N	N
4	F	9	46	280	Diffuse hemispheric glioma, NOS*	R/F-P	Y	Y	Y
5	M	16	65	154	Diffuse hemispheric glioma, NOS*	R/F-P	Y	N	Y
6	M	15	48	177	DMG, H3 K27-altered	Pons	Y	Y	Y
7	F	7	31	113	DMG, H3 K27-altered	Pons	N	N	N
8	M	15	76	186	DMG, H3 K27-altered	Mes	Y	Y	Y
9	F	8	28	145	DIPG	Pons	N	N	N
10	M	7	40	115	DMG, H3 K27-altered	Spinal cord	Y	Y	Y

DPHGG, diffuse paediatric-type high-grade glioma; *Y*, intense uptake; *N*, no uptake; *DMG*, diffuse midline glioma; *DIPG*, diffuse intrinsic pontine glioma; *Th*, thalamus; *R*, right; *F*, frontal; *Mes*, mesencephalon

*Molecular analyses were not available

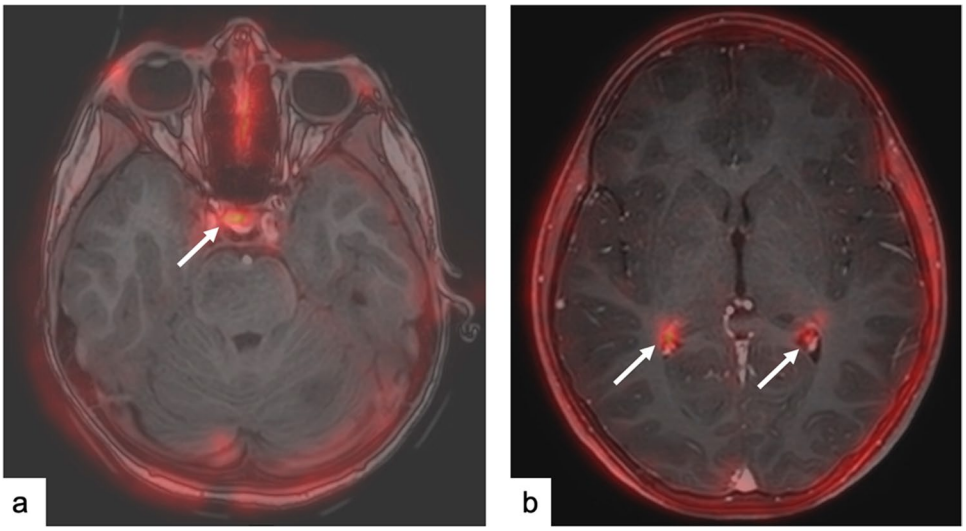

Fig. 1 **a**, **b** [^{64}Cu]$CuCl_2$ PET/MR imaging fusion. Physiological uptake of [^{64}Cu]$CuCl_2$ in normal brain structures outside the blood–brain barrier (pituitary gland and choroid plexus).

Regarding [^{64}Cu]$CuCl_2$ PET/MR imaging fusion, increased uptake was concordant with areas of contrast enhancement in all lesions, which, in some cases, was associated with ring enhancement. Infiltrative components without contrast enhancement did not show increased uptake (Table 2, Fig. 2). The [^{64}Cu]$CuCl_2$ uptake pattern was heterogeneous. Specifically, the highest avidity for [^{64}Cu]$CuCl_2$ was displayed in tumour areas with contrast enhancement along the margins of necrotic components (Fig. 3). Three non-necrotic contrast-enhancing areas displayed low uptake.

Five patients, with a total of seven areas with increased tracer uptake, underwent at least one further PET, 24 h after tracer injection; two of these five subjects (four lesions in total) underwent a third PET acquisition 72 h after the injection. In all these patients, the mean SUV increased over time (0.9 ± 0.5, 1.2 ± 0.7 and 1.8 ± 0.9 at the first, second and third time points, respectively). Likewise, mean TBR markedly increased over time (5.1 ± 3.5, 6.8 ± 3.7, and 11.3 ± 9.6). Subject 10's lesion, which was located in the thoracic spinal cord, had a lower TBR than the others, although the uptake was about average, owing to the higher background uptake caused by the proximity to the liver. See Table 3 for details.

[^{64}Cu]$CuCl_2$ Distribution in Normal Organs and Tumours

Among the organs considered, the liver showed the highest uptake (mean percent injected activity: 38.9%). By contrast,

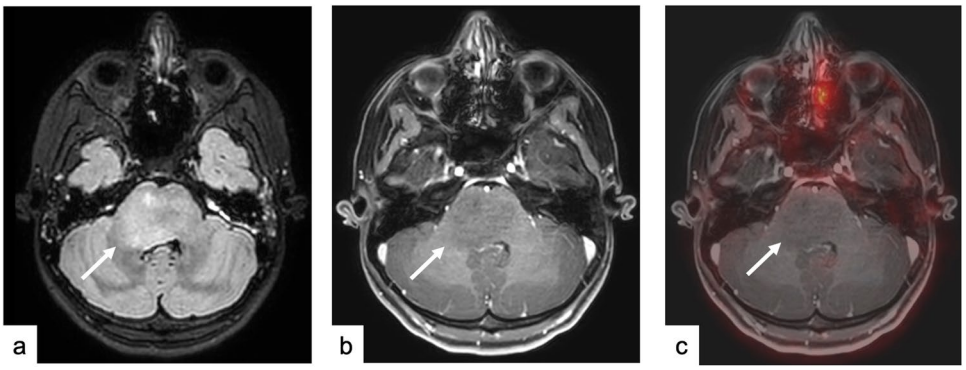

Fig. 2 **a** FLAIR image. **b** Post-contrast T1-weighted image. **c** [^{64}Cu]$CuCl_2$ PET/MR imaging fusion. Subject 9. Absence of tracer uptake in a non-enhancing diffuse intrinsic pontine glioma (arrows, **a**–**c**).

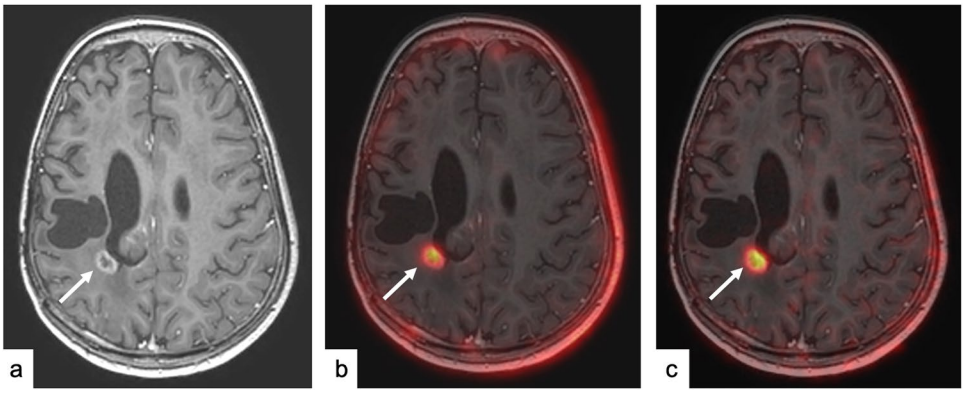

Fig. 3 **a** Post-contrast T1-weighted image. **b**, **c** [^{64}Cu]$CuCl_2$ PET/MR imaging fusion. Subject 4. Necrotic component displaying ring enhancement (arrow, **a**) with intense tracer uptake (arrow, **b**) in a diffuse hemispheric glioma. On later imaging 24 h after injection, the tracer intensity within the lesion had increased (arrow, **c**).

Table 3 Mean SUVmean and target-to-background ratio of all $^{64}CuCl_2$ positive lesions

Patient identifier	Volume (mL)	Site	SUV_{mean}			TBR		
			1 h	1 d	3 d	1 h	1 d	3 d
Subj. 1	6.8	Pons	0.4	0.8	1.2	3.4	4.5	4.5
Subj. 4	1.7	Hemi	1.4	2.1	2.5	10.0	12.0	18.0
Subj. 5	3.7	Hemi	0.3	0.3	-	3.2	3.8	-
Subj. 6	12.2	Pons	1.1	1.4	-	8.9	9.5	-
Subj. 8	1.1	Mes	0.8	1.1	-	3.4	4.1	-
Subj. 10	15.1	Med	1.3	-	-	1.6	-	-
Mean	4.7		0.9	1.1	1.9	5.1	6.8	11.3

all other organs displayed less marked tracer affinity, ranging from 0.17% (salivary glands) to 2.1% (kidneys). See Supplemental Fig. 1 for an outline. We also observed that the specific concentration depended on the patient's body weight, as can be seen from the decreasing trend in uptake with increasing weight in all organs (Fig. 2).

In general, the tumours showed moderate copper avidity, which was lower than that of most of the normal organs, except for the active bone marrow and the cerebral parenchyma. Figure 4 depicts the specific concentration of $[^{64}Cu]CuCl_2$ in the organs of all patients and the tumour concentration.

Dosimetry Estimates in Organs and Tumours

The liver displayed the highest normalised absorbed dose coefficient (6.39E-1 mGy/MBq), followed by the other abdominal organs (gallbladder, pancreas, kidneys and spleen). By contrast, the tumours received only 3.44E-2 mGy/MBq. However, the tumour dose coefficient was widely variable, ranging from 2.80E-5 (in a hemispheric DPHGG, H3-wildtype and IDH-wildtype) to 7.5E-2 mGy/MBq (in two pontine DPHGG, H3-wildtype and IDH-wildtype). Supplemental Fig. 2 and Table 4 depict these data.

The mean effective dose, according to the estimates provided by the ICRP protocols 60 and 103, was 6.51E-2 mSv/MBq and 6.10E-2 mSv/MBq, respectively.

Discussion

The present data are the result of what is, to the best of our knowledge, the first attempt to evaluate the potential diagnostic role, the biodistribution and the dosimetry of $[^{64}Cu]CuCl_2$ PET/CT in paediatric patients with diffusely infiltrating gliomas. In PDHGG, including diffuse pontine lesion, this radiopharmaceutical shows a characteristic distribution within tumours. Increased uptake was observed in paediatric gliomas with contrast-enhancing foci on MRI, and, in some cases, correlated with radiological evidence of tumour necrosis on MR imaging. This pattern is in line with previous preclinical and clinical studies performed by Pérès et al. [42] and Tateishi K et al. [43]. However, the extent of MRI contrast-enhancing areas with concomitant $[^{64}Cu]CuCl_2$ increased uptake was limited in comparison with non-enhancing infiltrative components (T2/FLAIR tumour extension), and four out of ten subjects (40%) with entirely non-enhancing high-grade gliomas did not show increased tracer uptake. Indeed, this radiopharmaceutical underestimates the overall extent of PDHHG in comparison with amino-acid PET tracers such as ^{18}F-DOPA [44–46]. However, the kinetic characteristics of $[^{64}Cu]CuCl_2$ make this element potentially suitable for late imaging, dosimetry and targeted therapy.

In positive lesions, the $[^{64}Cu]CuCl_2$ uptake pattern was mixed. This could be due to differences in tumour-specific biological variables, and might indicate a heterogeneous oxygen micro-environment [43[]. At the same time, since $[^{64}Cu]CuCl_2$ uptake was concordant with contrast enhancement on MRI, blood–brain barrier damage seems to be a potential prerequisite for the concentration of this tracer within lesions. Nevertheless, the significant increase in mean SUV over time in positive lesions suggests that a simple passive mechanism of uptake due to loss of integrity of the blood–brain barrier is unlikely. The contrast-enhancing MRI pattern seen in our population is in line with the findings of previous multicentre studies of both paediatric non-brainstem high-grade gliomas (HERBY study) [47] and DIPG [48], in which imaging showed little or no enhancement in 33% and 36% of lesions, respectively.

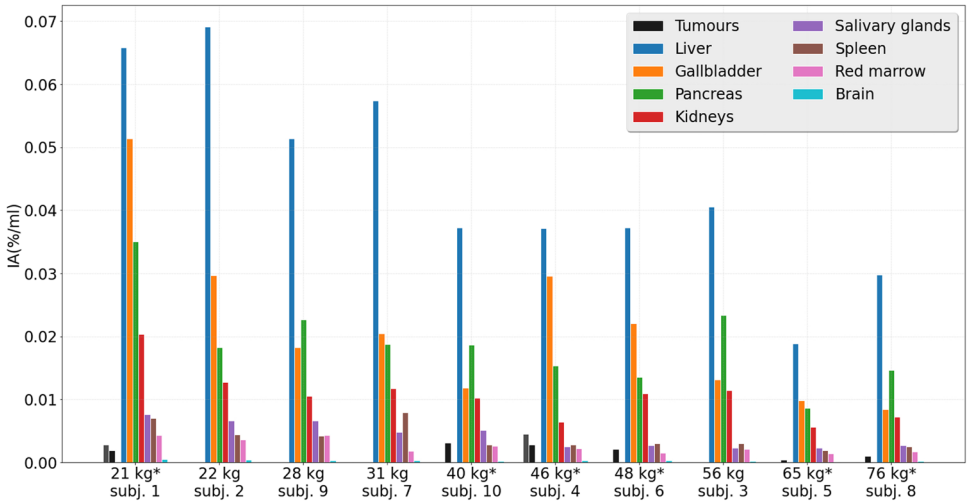

Fig. 4 $[^{64}Cu]CuCl_2$-specific uptake (% activity/mL) in organs and tumours.

Table 4 Absorbed dose coefficients of [^{64}Cu]CuCl$_2$. Mean values over the patients are also displayed, together with the standard deviation

Organ	Absorbed dose coefficient (mGy/MBq)					
	Pt 1 F 21 kg	Pt 4 F 46 kg	Pt 5 M 65 kg	Pt 6 M 48 kg	Pt 8 M 76 kg	Mean
Adrenals	9.48E-02	5.24E-02	3.70E-02	5.22E-02	3.27E-02	5.38E-02 ± 2.45E-02
Brain	1.06E-02	5.84E-03	2.80E-03	5.08E-03	3.77E-03	5.62E-03 ± 3.03E-03
Breasts	5.49E-02	2.31E-02	1.95E-02	2.95E-02	1.66E-02	2.87E-02 ± 1.54E-02
Gallbladder wall	6.44E-01	2.52E-01	9.89E-02	1.87E-01	8.57E-02	2.54E-01 ± 2.29E-01
LLI wall	5.69E-02	2.13E-02	2.05E-02	3.10E-02	1.79E-02	2.95E-02 ± 1.61E-02
Small intestine	7.28E-02	3.07E-02	2.53E-02	3.79E-02	2.15E-02	3.77E-02 ± 2.06E-02
Stomach wall	7.69E-02	3.35E-02	2.63E-02	3.87E-02	2.32E-02	3.97E-02 ± 2.16E-02
ULI wall	7.94E-02	3.62E-02	2.74E-02	4.05E-02	2.34E-02	4.14E-02 ± 2.23E-02
Heart wall	7.71E-02	3.85E-02	2.84E-02	4.20E-02	2.39E-02	4.20E-02 ± 2.10E-02
Kidneys	2.94E-01	1.08E-01	8.97E-02	1.54E-01	1.28E-01	1.55E-01 ± 8.16E-02
Liver	1.08E + 00	6.94E-01	3.34E-01	5.88E-01	5.02E-01	6.39E-01 ± 2.78E-01
Lungs	6.77E-02	3.29E-02	2.56E-02	3.74E-02	2.18E-02	3.71E-02 ± 1.82E-02
Muscle	5.74E-02	2.39E-02	2.12E-02	3.16E-02	1.81E-02	3.04E-02 ± 1.59E-02
Ovaries	6.23E-02	2.45E-02	-	-	-	4.34E-02 ± 2.67E-02
Pancreas	3.91E-01	1.79E-01	1.10E-01	1.94E-01	1.46E-01	2.04E-01 ± 1.09E-01
Red marrow	5.03E-02	3.07E-02	1.37E-02	1.60E-02	1.60E-02	2.54E-02 ± 1.55E-02
Osteogenic cells	8.39E-02	4.03E-02	3.10E-02	4.42E-02	2.76E-02	4.54E-02 ± 2.25E-02
Skin	4.89E-02	1.90E-02	1.75E-02	2.65E-02	1.50E-02	2.54E-02 ± 1.38E-02
Spleen	1.62E-01	5.62E-02	3.74E-02	5.55E-02	4.28E-02	7.07E-02 ± 5.14E-02
Testes	-	-	1.80E-02	2.74E-02	1.52E-02	2.02E-02 ± 6.39E-03
Thymus	5.67E-02	2.30E-02	2.11E-02	3.15E-02	1.78E-02	3.00E-02 ± 1.57E-02
Thyroid	5.39E-02	1.94E-02	1.90E-02	2.93E-02	1.60E-02	2.75E-02 ± 1.56E-02
Urinary bladder wall	5.63E-02	2.04E-02	2.01E-02	3.00E-02	1.75E-02	2.89E-02 ± 1.61E-02
Uterus	6.21E-02	2.41E-02	-	-	-	4.31E-02 ± 2.69E-02
Salivary glands	6.46E-02	2.61E-02	1.38E-01	3.23E-02	2.74E-02	5.77E-02 ± 4.76E-02
Total body	9.39E-02	4.68E-02	3.15E-02	4.64E-02	2.72E-02	4.92E-02 ± 2.65E-02
Effective dose ICRP 60 (mSv/MBq)	1.19E-01	6.35E-02	3.82E-02	5.94E-02	4.51E-02	6.51E-02 ± 3.19E-02
Effective dose ICRP 103 (mSv/MBq)	1.13E-01	5.84E-02	3.66E-02	5.66E-02	4.07E-02	6.10E-02 ± 3.05E-02

Negative [^{64}Cu]CuCl$_2$ PET/CT lesions were all located in the midline. According to the 2016 and 2021 WHO classifications, these lesions are categorised as WHO grade IV, based on their molecular profile, including histologically low-grade H3K27-altered diffuse astrocytomas. In this context, accelerated cell proliferation could be variably present [49, 50]. Therefore, midline tumours with mild-to-moderate proliferation indices may not exhibit copper avidity, even in the presence of a diffusely infiltrating indicating a dire prognosis. On the other hand, the highest uptake was shown by a hemispheric PDHGG with a histological diagnosis of glioblastoma, which normally exhibits characteristics linked with accelerated proliferation [51].

Our study adds further insight into copper kinetics, in that the standardised uptake values increased over time, up to 3 days after administration. This pattern suggests that once incorporated, [^{64}Cu]CuCl$_2$ does not leave the tumour cells; such a prolonged accumulation is probably typical of gliomas since our previous experience with prostate cancer documented rapid clearance in the first hour after the maximum uptake [31].

Overall, on the basis of this pilot study, we suggest that [^{64}Cu]CuCl$_2$ PET/CT might be selectively used in paediatric gliomas showing contrast enhancement in the whole tumour volume; in such lesions, the prolonged accumulation might constitute the rationale for potential theranostic use. However, further larger studies are needed to test this concept. Specifically, in paediatric patients with BRAF V600E-mutant gliomas—a distinctive clinical-biological group of paediatric gliomas which typically present a contrast-enhancing MRI pattern—the role of [^{64}Cu]CuCl$_2$ in patients who do not respond to current

treatment regimens [52] could be explored, given that copper is required for oncogenic BRAF signalling and tumorigenesis [23]. As demonstrated in a previous multicentre study of BRAF V600E-mutant paediatric high-grade gliomas, new strategies beyond BRAF-inhibitor monotherapy are needed [52].

From the dosimetry point of view, should a theranostic approach be considered, the liver is the limiting organ. Indeed, our analysis showed that, on average, the liver received about twenty times more energy than the tumour per MBq employed. However, previous evidence suggests that the ^{64}Cu-mediated cell damage is dependent on the emission of Auger electrons, with this specific component delivering up to a 25-fold higher dose than beta radiation [31, 53, 54]. Given the low range of Auger electrons, the dose actually absorbed by the cell depends on whether the radiopharmaceutical is absorbed into the cell nucleus or not [55]. Should the tracer remain in the hepatic cell cytoplasm, then the dose absorbed by the liver cell would be determined by the beta components mainly, which could be less limiting in the therapeutic use of the radiopharmaceutical, especially if we also consider the relative resilience of the liver [56]. An ideal scenario for the theranostic application of [^{64}Cu]$CuCl_2$ would be one of intra-nuclear absorption in the tumour cells and a cytoplasmatic distribution in non-target tissue. Such an evaluation, however, requires the set-up of targeted experiments.

Finally, the dosimetry information provided by this study could be carried over to other disease settings. Particularly, the potential of this tracer could be evaluated in neuroblastoma, which is the most frequent extracranial neoplasm and whose cells express a copper transporter, playing a role in chemotherapy sensitivity [57–59].

Some limitations of this study must be borne in mind. Being a pilot, project aimed mainly at assessing the feasibility, tolerability and dosimetry of [^{64}Cu]$CuCl_2$ in children, it involved only a small number of patients. Moreover, as many of these patients had a midline glioma, the amount of data available on hemispheric glial tumours was limited. Finally, we did not have information on the late phase of all lesions in all patients, since ethics considerations prevented us from carrying out repeated imaging in cases without visible tracer uptake on the first examination.

Conclusions

[^{64}Cu]$CuCl_2$ is a safe tracer in the imaging of paediatric gliomas. It is selectively taken up by MRI contrast-enhancing/necrotic tumours, suggesting that blood–brain barrier damage is a prerequisite for tracer uptake. Moreover, this radiopharmaceutical shows excellent target-to-background contrast and an accumulating pattern over time. The possibility of employing this radiopharmaceutical for therapeutic applications could represent the subject of further research.

Supplementary Information.

Supplementary Information The online version contains supplementary material available at https://doi.org/10.1007/s11307-022-01769-3.

Funding This work was supported by the Italian Ministry of Health and by Regione Liguria "Ricerca Finalizzata di Rete NET-2019–12371188 GLI-HOPE".

Declarations

Conflict of Interest The authors declare no competing interests.

References

1. Blionas A, Giakoumettis D, Klonou A et al (2018) Paediatric gliomas: diagnosis, molecular biology and management. Ann Transl Med 6:251
2. Immanuel V, Kingsley PA, Negi P et al (2017) Variegated colors of pediatric glioblastoma multiforme: what to expect? Rare Tumors 9:6552
3. Rashed WM, Maher E, Adel M et al (2019) Pediatric diffuse intrinsic pontine glioma: where do we stand? Cancer Metastasis Rev 38:759–770
4. Louis DN, Perry A, Wesseling P et al (2021) The 2021 WHO classification of tumors of the central nervous system: a summary. Neuro Oncol 23:1231–1251
5. Ansari M, Nasrolahi H, Kani AA et al (2012) Pediatric glioblastoma multiforme: a single-institution experience. Indian J Med Paediatr Oncol 33:155–160
6. Konar SK, Bir SC, Maiti TK et al (2017) A systematic review of overall survival in pediatric primary glioblastoma multiforme of the spinal cord. J Neurosurg Pediatr 19:239–248
7. Boudaouara O, Charfi S, Bahri M et al (2019) Pediatric high grade gliomas: clinico-pathological profile, therapeutic approaches and factors affecting overall survival. Neurochirurgie 65:63–68
8. Grimm SA, Chamberlain MC (2013) Brainstem glioma: a review. Curr Neurol Neurosci Rep 13:346
9. Felker J, Broniscer A (2020) Improving long-term survival in diffuse intrinsic pontine glioma. Expert Rev Neurother 20:647–658
10. Covarrubias G, Johansen ML, Vincent J et al (2020) PTPmu-targeted nanoparticles label invasive pediatric and adult glioblastoma. Nanomedicine 28:102216
11. Lieberman NAP, DeGolier K, Kovar HM et al (2019) Characterization of the immune microenvironment of diffuse intrinsic pontine glioma: implications for development of immunotherapy. Neuro Oncol 21:83–94
12. Shabason JE, Sutton D, Kenton O et al (2016) Patterns of failure for pediatric glioblastoma multiforme following radiation therapy. Pediatr Blood Cancer 63:1465–1467
13. Fangusaro J (2012) Pediatric high grade glioma: a review and update on tumor clinical characteristics and biology. Front Oncol 2:105
14. Cohen KJ, Pollack IF, Zhou T et al (2011) Temozolomide in the treatment of high-grade gliomas in children: a report from the Children's Oncology Group. Neuro Oncol 13:317–323
15. Janssens GO, Jansen MH, Lauwers SJ et al (2013) Hypofractionation vs conventional radiation therapy for newly diagnosed diffuse intrinsic pontine glioma: a matched-cohort analysis. Int J Radiat Oncol Biol Phys 85:315–320

16. Janssens GO, Gandola L, Bolle S et al (2017) Survival benefit for patients with diffuse intrinsic pontine glioma (DIPG) undergoing re-irradiation at first progression: a matched-cohort analysis on behalf of the SIOP-E-HGG/DIPG working group. Eur J Cancer 73:38–47
17. Janjua MB, Ban VS, El Ahmadieh TY et al (2020) Diffuse intrinsic pontine gliomas: diagnostic approach and treatment strategies. J Clin Neurosci 72:15–19
18. Katagi H, Louis N, Unruh D et al (2019) Radiosensitization by Histone H3 demethylase inhibition in diffuse intrinsic pontine glioma. Clin Cancer Res 25:5572–5583
19. Christensen M, Kamson DO, Snyder M et al (2014) Tryptophan PET-defined gross tumor volume offers better coverage of initial progression than standard MRI-based planning in glioblastoma patients. J Radiat Oncol 3:131–138
20. Law I, Albert NL, Arbizu J et al (2019) Joint EANM/EANO/RANO practice guidelines/SNMMI procedure standards for imaging of gliomas using PET with radiolabelled amino acids and [(18)F]FDG: version 1.0. Eur J Nucl Med Mol Imaging 46:540–557
21. Huskisson E, Maggini S, Ruf M (2007) The role of vitamins and minerals in energy metabolism and well-being. J Int Med Res 35:277–289
22. Horn D, Barrientos A (2008) Mitochondrial copper metabolism and delivery to cytochrome c oxidase. IUBMB Life 60:421–429
23. Brady DC, Crowe MS, Turski ML et al (2014) Copper is required for oncogenic BRAF signalling and tumorigenesis. Nature 509:492–496
24. Ishida S, Andreux P, Poitry-Yamate C et al (2013) Bioavailable copper modulates oxidative phosphorylation and growth of tumors. Proc Natl Acad Sci U S A 110:19507–19512
25. Shanbhag VC, Gudekar N, Jasmer K et al (2021) Copper metabolism as a unique vulnerability in cancer. Biochim Biophys Acta Mol Cell Res 1868:118893
26. Cui L, Gouw AM, LaGory EL et al (2021) Mitochondrial copper depletion suppresses triple-negative breast cancer in mice. Nat Biotechnol 39:357–367
27. Petruzzelli R, Polishchuk RS (2019) Activity and trafficking of copper-transporting ATPases in tumor development and defense against platinum-based drugs. Cells 8(9):1080
28. Williams HA, Robinson S, Julyan P et al (2005) A comparison of PET imaging characteristics of various copper radioisotopes. Eur J Nucl Med Mol Imaging 32:1473–1480
29. Bolzati C, Duatti A (2020) The emerging value of 64Cu for molecular imaging and therapy. Q J Nucl Med Mol Imaging 64:329–337
30. Bé MM, Cassette P, Lépy MC et al (2012) Standardization, decay data measurements and evaluation of 64Cu. Appl Radiat Isot 70:1894–1899
31. Righi S, Ugolini M, Bottoni G et al (2018) Biokinetic and dosimetric aspects of (64)CuCl(2) in human prostate cancer: possible theranostic implications. EJNMMI Res 8:18
32. Panichelli P, Villano C, Cistaro A et al (2016) Imaging of brain tumors with copper-64 chloride: early experience and results. Cancer Biother Radiopharm 31:159–167
33. McCarthy DW, Shefer RE, Klinkowstein RE et al (1997) Efficient production of high specific activity 64Cu using a biomedical cyclotron. Nucl Med Biol 24:35–43
34. ICRP (1995) Basic anatomical & physiological data for use in radiological protection: the skeleton: the Skeleton. ICRP Publication 70. Ann ICRP 25:1–80
35. Siegel JA, Thomas SR, Stubbs JB et al (1999) MIRD pamphlet no. 16: techniques for quantitative radiopharmaceutical biodistribution data acquisition and analysis for use in human radiation dose estimates. J Nucl Med 40:37s–61s
36. Loeevinger R, Berman M (1968) A schema for absorbed-dose calculations for biologically-distributed radionuclides. J Nucl Med. Suppl 1:9–14
37. Snyder W, Ford, Warner GG, et al (1975) MIRD Pamphlet #11: S, absorbed dose per unit cumulated activity for selected radionuclides and organs
38. Stabin MG, Sparks RB, Crowe E (2005) OLINDA/EXM: the second-generation personal computer software for internal dose assessment in nuclear medicine. J Nucl Med 46:1023–1027
39. ICRP (2007) The 2007 Recommendations of the International Commission on Radiological Protection (2007) ICRP publication 103. Ann ICRP 37:1–332
40. ICRP (1991) 1990 Recommendations of the International Commission on Radiological Protection. ICRP Publication 60. Ann ICRP 21:1–3
41. Cooney TM, Cohen KJ, Guimaraes CV et al (2020) Response assessment in diffuse intrinsic pontine glioma: recommendations from the Response Assessment in Pediatric Neuro-Oncology (RAPNO) working group. Lancet Oncol 21:e330–e336
42. Pérès EA, Toutain J, Paty LP et al (2019) (64)Cu-ATSM/(64)Cu-Cl(2) and their relationship to hypoxia in glioblastoma: a preclinical study. EJNMMI Res 9:114
43. Tateishi K, Tateishi U, Nakanowatari S et al (2014) (62)Cu-diacetyl-bis (N(4)-methylthiosemicarbazone) PET in human gliomas: comparative study with [(18)F]fluorodeoxyglucose and L-methyl-[(11)C]methionine PET. AJNR Am J Neuroradiol 35:278–284
44. Morana G, Piccardo A, Tortora D et al (2017) Grading and outcome prediction of pediatric diffuse astrocytic tumors with diffusion and arterial spin labeling perfusion MRI in comparison with 18F-DOPA PET. Eur J Nucl Med Mol Imaging 44:2084–2093
45. Morana G, Tortora D, Bottoni G et al (2020) Correlation of multimodal (18)F-DOPA PET and conventional MRI with treatment response and survival in children with diffuse intrinsic pontine gliomas. Theranostics 10:11881–11891
46. Piccardo A, Tortora D, Mascelli S et al (2019) Advanced MR imaging and (18)F-DOPA PET characteristics of H3K27M-mutant and wild-type pediatric diffuse midline gliomas. Eur J Nucl Med Mol Imaging 46:1685–1694
47. Grill J, Massimino M, Bouffet E et al (2018) Phase II, Open-label, randomized, multicenter trial (HERBY) of bevacizumab in pediatric patients with newly diagnosed high-grade glioma. J Clin Oncol 36:951–958
48. Jansen MH, Veldhuijzen van Zanten SE, Sanchez Aliaga E et al (2015) Survival prediction model of children with diffuse intrinsic pontine glioma based on clinical and radiological criteria. Neuro Oncol 17:160–166
49. Thust S, Micallef C, Okuchi S et al (2021) Imaging characteristics of H3 K27M histone-mutant diffuse midline glioma in teenagers and adults. Quant Imaging Med Surg 11:43–56
50. Leach JL, Roebker J, Schafer A et al (2020) MR imaging features of diffuse intrinsic pontine glioma and relationship to overall survival: report from the International DIPG Registry. Neuro Oncol 22:1647–1657
51. Colwell N, Larion M, Giles AJ et al (2017) Hypoxia in the glioblastoma microenvironment: shaping the phenotype of cancer stem-like cells. Neuro Oncol 19:887–896
52. Nobre L, Zapotocky M, Ramaswamy V, et al (2020) Outcomes of BRAF V600E pediatric gliomas treated with targeted BRAF inhibition. JCO Precis Oncol 4:PO.19.00298
53. Chan PC, Lisco E, Lisco H et al (1976) The radiotoxicity of iodine-125 in mammalian cells II. A comparative study on cell survival and cytogenetic responses to 125IUdR, 131TUdR, and 3HTdR. Radiat Res 67:332–343

54. Kassis AI, Adelstein SJ, Haydock C et al (1982) Lethality of Auger electrons from the decay of bromine-77 in the DNA of mammalian cells. Radiat Res 90:362–373
55. Kassis AI, Sastry KS, Adelstein SJ (1985) Intracellular distribution and radiotoxicity of chromium-51 in mammalian cells: Auger-electron dosimetry. J Nucl Med 26:59–67
56. Piccardo A, Paparo F, Puntoni M et al (2018) (64)CuCl(2) PET/CT in prostate cancer relapse. J Nucl Med 59:444–451
57. Bohlken A, Cheung BB, Bell JL et al (2009) ATP7A is a novel target of retinoic acid receptor β2 in neuroblastoma cells. Br J Cancer 100:96–105
58. Parmar A, Pascali G, Voli F et al (2018) In vivo [64 Cu]CuCl 2 PET imaging reveals activity of Dextran-Catechin on tumor copper homeostasis. Theranostics 8:5645–5659
59. Kilari D, Icykowski KA, Pandya C et al (2016) copper transporter-CTR1 expression and pathological outcomes in platinum-treated muscle-invasive bladder cancer patients. Anticancer Res 36:495–501

Authors and Affiliations

Francesco Fiz[1] · Gianluca Bottoni[1] · Martina Ugolini[1] · Sergio Righi[2] · Alessio Cirone[2] · Maria Carmen Garganese[3] · Antonio Verrico[4] · Andrea Rossi[5,6] · Claudia Milanaccio[4] · Antonia Ramaglia[5] · Angela Mastronuzzi[7] · Massimo Eraldo Abate[8] · Antonella Cacchione[7] · Carlo Gandolfo[9] · Giovanna Stefania Colafati[9] · Maria Luisa Garrè[4] · Giovanni Morana[10] · Arnoldo Piccardo[1]

1 Department of Nuclear Medicine, E.O. Ospedali Galliera, Galliera Hospital, Mura delle Cappuccine 14, 16128 Genoa, Italy

2 Medical Physics Department, E.O. Galliera Hospital, Genoa, Italy

3 Nuclear Medicine Unit/Imaging Department, IRCCS Bambino Gesù Children's Hospital, Rome, Italy

4 Neuro-Oncology Unit, IRCCS Istituto Giannina Gaslini, Genoa, Italy

5 Neuroradiology Unit, IRCCS Istituto Giannina Gaslini, Genoa, Italy

6 Department of Health Sciences (DISSAL), University of Genoa, Genoa, Italy

7 Neuro-Oncology Unit, Department of Paediatric Haematology/Oncology, Cell Therapy, Gene Therapies and Hemopoietic Transplant, Bambino Gesù Children's Hospital, IRCCS, 00165 Rome, Italy

8 Pediatric Oncology Unit, AORN Santobono-Pausilipon Hospital, Naples, Italy

9 Imaging Department, Neuroradiology Unit, IRCCS Bambino Gesù Children's Hospital, Rome, Italy

10 Department of Neurosciences, University of Turin, Turin, Italy